# Disentangling uterine and bladder activity in paired EHG-MRI data using anatomy-guided multicluster beamforming

Maria Camila Bustos-Vivas[1], Smiti Tripathy[1], Jordina Aviles Verdera[2], Nyvenn Alves de Castro[1], and Jana Hutter[2]

[1] Radiology Department, Uniklinikum Erlangen, Krankenhausstr. 12, 91054 Erlangen, Germany
[2] Institut für Informationsverarbeitung, Leibniz University Hannover, Appelstr. 11A, 30167 Hannover, Germany

**Abstract.** The intrinsic motion of the human uterus is key both for healthy physiology and for the etiology of diseases such as endometriosis and adenomyosis. However, non-invasive characterization remains a major challenge due to the location of the uterus, low signal-to-noise and overlapping motion from adjacent organs. Electrohysterography (EHG) is a method for monitoring uterine contractility using a surface electrode array. Previous studies that combined EHG and Magnetic Resonance Imaging (MRI) to analyze uterine peristalsis assumed an empty bladder, neglecting the influence of bladder filling. The overlap of uterine and bladder frequency ranges results however in frequency filtering alone being insufficient for uterine signal isolation. We introduce a novel multi-cluster beamforming framework based on simultaneous EHG and MRI to separate uterine and bladder electrical activity. Subject-specific 3D segmentations of the uterus, bladder, and electrodes enabled the generation of volumetric lead-field dictionaries, cluster-geometry-based DOA vectors, and spatially coherent organ-specific clusters. These clusters defined uterus-pass and bladder-null constraints in a multicluster linearly constrained minimum-variance (LCMV) beamformer with Bayesian covariance shrinkage, followed by overlap-add reconstruction of organ-resolved time series. Paired T1-weighted 3D whole abdomen MRI and multi-channel EHG data from 10 volunteers (7 females and 3 males), including longitudinal data from 3 women across menstrual phases was acquired. Raw EHG signals showed activity in the $[5, 50]$ mHz band; in men only bladder components $[25, 41]$ mHz were present, while female datasets exhibited uterine and bladder contributions. Across female volunteers, uterus–bladder separation angles varied (13°–38°), but cluster compactness strongly predicted beamformer stability (Pearson $r = 0.91$; Spearman $\rho = 0.89$). Leakage subtraction consistently improved bladder isolation. The proposed anatomy-guided multicluster LCMV enables robust uterus–bladder signal separation in low-channel EHG.

**Keywords:** Uterine Peristalsis · Electrohysterography · Beamforming · MRI.

## 1 Introduction

Electrohysterography (EHG) is a non-invasive technique for recording myometrial electrical activity [4, 7], particularly during uterine muscular activity. This activity, often referred to as uterine peristalsis, exhibits distinct variations in frequency, intensity, and directionality throughout the menstrual cycle [3, 8, 13]. Peristalsis is fundamental to reproductive health, concretely to physiological processes including menstruation, sperm transport, and implantation [9]. Furthermore, deviations from established patterns can carry significant clinical implications [11]. Abnormal uterine contractility, specifically hypercontractility, is frequently linked to pathologies such as adenomyosis, endometriosis, and leiomyoma [5–7]. Unlike invasive intrauterine pressure catheters or imaging modalities with limited temporal accessibility, EHG offers a viable pathway for continuous, non-invasive monitoring [4, 5], resulting in growing research interest [1, 10, 13].

Electrical source imaging techniques and inverse methods from magnetoencephalography (MEG) have been adapted to reconstruct uterine activity during pregnancy [15, 16]. Leveraging the strong, synchronized, and spatially extended pregnancy contractions thereby facilitates inverse reconstruction despite the ill-posed nature of the problem. More recently, electromyometrial imaging (EMMI) has been adapted to the non-pregnant uterus, using high-density surface recordings combined with patient-specific geometry to reconstruct 3D activation patterns [12, 13]. However, contamination from adjacent organs—particularly the bladder, which occupies a nearly identical low-frequency band—remains a key limitation. This spectral overlap makes frequency filtering insufficient and motivates the use of Linearly Constrained Minimum-Variance (LCMV) beamforming. Although widely applied in neuroscience and cardiac electrophysiology, such beamformers have not yet been adapted to the anatomical complexity and depth of the female pelvis. Advanced Bayesian frameworks, including Bayesian Principal Component Analysis [14] and Bayesian adaptive beamformers [2], further provide robust covariance regularization for isolating overlapping generators.

In this work, we introduce the first anatomy-guided multicluster beamforming framework to separate uterine and bladder electrical activity using simultaneous EHG and MRI. The contributions are threefold: (1) we construct subject-specific, volumetric lead-field and direction-of-arrival (DOA)-based steering dictionaries from 3D MRI; (2) we design a multi-cluster LCMV beamformer with organ-specific pass and null constraints, combined with Bayesian covariance shrinkage; and (3) we perform in-vivo validation in 10 participants demonstrating reliable uterus–bladder separation under an 8-channel EHG configuration.

## 2 Methods

### 2.1 Setup and Acquisition Protocol

Anatomic uterine MRI was acquired using a 0.55T MAGNETOM Free.Max MRI (Siemens Healthineers, Germany) with a 9ch contour coil while recording synchronized transabdominal EMG signals at a sampling rate of 5 kHz via an 8ch

BrainAmp ExG MR with special MRI-conditional multirode bipolar electrodes (Brain Products, Germany). The surface coil was placed above the electrodes, keeping the BrainAmp ExG MR outside the bore. Skin preparation was performed with abrasive gel to reduce electrode impedance below 10 kΩ. Basic demographic information was provided.

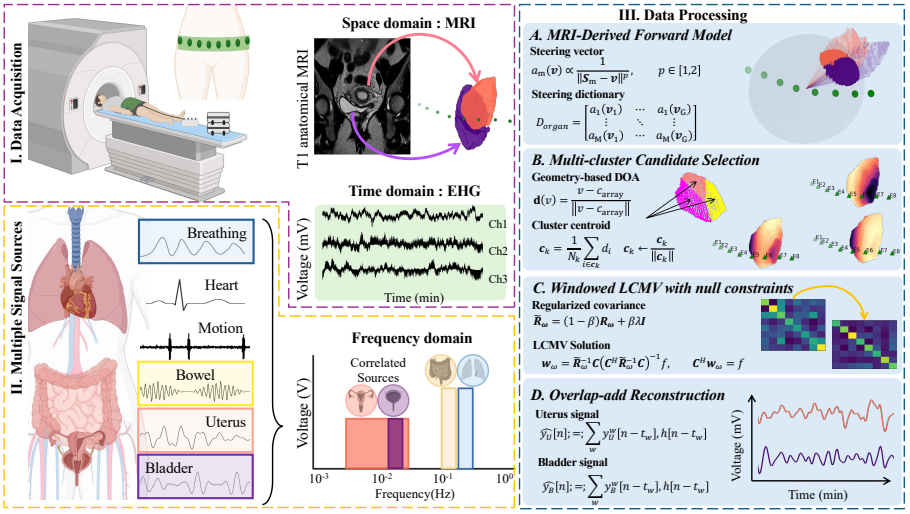


**Fig. 1. Proposed pipeline. I.** Simultaneous EHG and T1-weighted MRI provide time-, frequency-, and spatial-domain information. **II.** Conceptual illustration of correlated sources of abdominal EHG. **III.** The MRI-derived forward model generates steering vectors, and geometry-based DOA clustering identifies multi-cluster organ-specific candidates. Windowed LCMV beamforming with organ-specific null constraints. Time-domain signals are reconstructed using Hann overlap-add.

## 2.2 Multi-constraint LCMV beamformer and signal reconstruction

EHG recordings contain a mixture of uterine and bladder activity whose ultra–low–frequency components overlap. In a linear mixing model $\mathbf{x}(t) = \mathbf{A}\mathbf{s}(t) + \boldsymbol{\varepsilon}(t)$ with source vector $\mathbf{s}(t)$ and forward matrix $\mathbf{A}$, overlapping spectra imply that any frequency mapping $\Phi(\mathbf{x}(t))$ satisfies $\Phi(\mathbf{A}\mathbf{s}(t)) \approx \Phi(\mathbf{x}(t))$, leaving the origin of each component ambiguous. Since frequency-domain criteria provide no reliable separation, spatial structure must constrain the inverse problem:

**MRI-Derived Forward Model:** 3D organ meshes and electrode array geometry are obtained from segmented $T_1$ MRI datasets. The anatomical vertices of the meshes define the candidate source locations $G_U$ and $G_B$, respectively. Given electrode locations $\mathbf{r}_i \in \mathbb{R}^3$ and a vertex $\mathbf{r} \in \mathbb{R}^3$ on a segmented organ mesh, the

steering vector assigned to each vertex follows a quasi-static bio-electric conduction model as $a_i(\mathbf{r}) \propto \|\mathbf{r}_i - \mathbf{r}\|^{-p} \in \mathbb{C}^M$ with $p \in [1, 2]$. After $\ell_2$-normalization, stacking these vectors yields uterus and bladder steering dictionaries $\mathbf{D}_U = [\,\mathbf{a}(\mathbf{r}_1^U) \cdots \mathbf{a}(\mathbf{r}_{G_U}^U)\,] \in \mathbb{C}^{M \times G_U}$ and $\mathbf{D}_B = [\,\mathbf{a}(\mathbf{r}_1^B) \cdots \mathbf{a}(\mathbf{r}_{G_B}^B)\,] \in \mathbb{C}^{M \times G_B}$. The $M$-channel EHG at time $t$ is defined as a linear superposition of anatomy plus noise $\mathbf{x}(t) = \sum_k \mathbf{a}(\mathbf{r}_k) s_k(t) + \boldsymbol{\varepsilon}(t) \in \mathbb{R}^M$ which undergoes band-limited processing in uterus $[5 - 50]mHz$ and bladder $[25 - 41]mHz$ ranges [13].

**Multi-cluster Candidate Selection:** Directional hypotheses arise from mapping each anatomical vertex to a unit DOA vector as $\mathbf{d}(\mathbf{r}) = (\mathbf{r} - \mathbf{c}_{\text{array}})/\|\mathbf{r} - \mathbf{c}_{\text{array}}\| \in \mathbb{R}^3$ where $\mathbf{c}_{\text{array}} \in \mathbb{R}^3$ is the electrode array geometric center. Directional clustering separate uterus and bladder DOAs into groups. Each cluster centroid takes the form $\mathbf{c}_k = (\sum_{\mathbf{d}_i \in \mathcal{C}_k} \mathbf{d}_i)/\big\|\sum_{\mathbf{d}_i \in \mathcal{C}_k} \mathbf{d}_i\big\| \in \mathbb{R}^3$ and represents a dominant organ-specific propagation direction. Normalized averaging of member steering vectors maps each cluster $\mathcal{C}_k$ back to sensor space to produce representative steering vectors

$$\mathbf{s}_k \;=\; \frac{1}{|\mathcal{C}_k|} \sum_{\mathbf{r}_i \in \mathcal{C}_k} \frac{\mathbf{a}(\mathbf{r}_i)}{\|\mathbf{a}(\mathbf{r}_i)\|_2} \;\Bigg/\; \left\| \frac{1}{|\mathcal{C}_k|} \sum_{\mathbf{r}_i \in \mathcal{C}_k} \frac{\mathbf{a}(\mathbf{r}_i)}{\|\mathbf{a}(\mathbf{r}_i)\|_2} \right\|_2 .$$

Collecting uterus (pass) and bladder (null) cluster representatives produces $\mathbf{S}^{(U)} = \big[\mathbf{s}_1^{(U)} \cdots \mathbf{s}_{K_U}^{(U)}\big] \in \mathbb{C}^{M \times K_U}$, $\mathbf{S}^{(B)} = \big[\mathbf{s}_1^{(B)} \cdots \mathbf{s}_{K_B}^{(B)}\big] \in \mathbb{C}^{M \times K_B}$.

**Windowed LCMV with Null Constraints:** Band-limited data segments define the window $w$ with samples $\mathbf{x}[n]_{n=1}^{N_w}$, the sample covariance and a shrinkage-regularized version are

$$\mathbf{R}_w \;=\; \frac{1}{N_w} \sum_{n=1}^{N_w} \mathbf{x}[n]\mathbf{x}[n]^{\mathsf{H}} \in \mathbb{C}^{M \times M},$$

$$\tilde{\mathbf{R}}_w \;=\; (1 - \beta)\, \mathbf{R}_w \;+\; \beta\, \mathrm{diag}(\mathbf{R}_w) \in \mathbb{C}^{M \times M}, \quad \beta \in [0, 1]$$

Constraints enforce unity gain along uterus directions and zero gain along bladder directions. Constraint matrix incorporates uterus-pass and bladder-null directions as $\mathbf{C} = [\,\mathbf{s}_{\text{pass}}^{(U)} \;\; \mathbf{Q}_{\text{null}}^{(B)}\,] \in \mathbb{C}^{M \times L}$ with targets $\mathbf{f} = [1, 0, \ldots, 0]^{\mathsf{T}} \in \mathbb{C}^L$. The LCMV solution for window $w$ follows the standard form:

$$\mathbf{w}_w = \tilde{\mathbf{R}}_w^{-1}\mathbf{C}\big(\mathbf{C}^{\mathsf{H}}\tilde{\mathbf{R}}_w^{-1}\mathbf{C}\big)^{-1}\mathbf{f} \in \mathbb{C}^M, \mathbf{C}^{\mathsf{H}}\mathbf{w}_w = \mathbf{f}$$

A symmetric bladder beamformer $\mathbf{w}_w^B$ is solved with swapped pass/null roles ($\mathbf{C}^B = [\,\mathbf{s}_{\text{pass}}^{(B)} \;\; \mathbf{Q}_{\text{null}}^{(U)}\,]$); denoting the uterus weights $\mathbf{w}_w^U$, band-limited outputs are $y_U^w[n] = (\mathbf{w}_w^U)^{\mathsf{H}}\mathbf{x}_U[n]$ and $y_B^w[n] = (\mathbf{w}_w^B)^{\mathsf{H}}\mathbf{x}_B[n]$. Constraints verifications are possible by $\delta = \mathbf{C}^{\mathsf{H}}\mathbf{w}_w - \mathbf{f}$ and monitoring its infinity norm $\|\delta\|_\infty$. Since the uterus pass response is normalized to unity, keeping $\|\delta\|_\infty \ll 1$ guarantees that deviations from the desired spatial response remain negligible relative to the target gain.

**Overlap–Add Reconstruction:** Each windowed output undergoes tapering by $h[n]$ and aligns to its temporal offset $t_w$ to form continuous uterus and bladder reconstructions

$$\hat{y}_U[n] \;=\; \sum_w y_U^w[n-t_w]\,h[n-t_w], \qquad \hat{y}_B[n] \;=\; \sum_w y_B^w[n-t_w]\,h[n-t_w].$$

Bladder beamformer output may retain a small contribution from the uterus due to imperfect nulling. A scalar leakage subtraction reduces cross-talk in the bladder trace. The leakage coefficient $\alpha = \mathrm{median}_w\big(\langle y_B^w,\, y_U^w\rangle / \langle y_U^w,\, y_U^w\rangle\big)$ estimates the uterus component. Subtraction ($\hat{y}_B[n] \;-\; \alpha\,\hat{y}_U[n]$) removes only the coherent uterus-like contamination while preserving the intrinsic bladder-band activity. Using a complex Morlet CWT to derive uterine scalograms $S_U(f,n) = \big|W_U(a_f,n)\big|^2$, $S_B(f,n) = \big|W_B(a_f,n)\big|^2$. $W_U$ and $W_B$ denote the CWT of $\hat{y}_U$ and $\hat{y}_B$ respectively, $a_f$ is the scale corresponding to frequency $f$. Band-powers are

$$P_U[n] \;=\; \sum_{f\in\mathcal{B}_U} S_U(f,n), \qquad P_B[n] \;=\; \sum_{f\in\mathcal{B}_B} S_B(f,n), \tag{1}$$

and a separation metric is given by the ratio $\rho[n] \;=\; P_U[n]/(P_B[n]+\varepsilon), \quad \varepsilon > 0$. Geometric (separation, compactness), constraint (pass/null gains, residuals), and reconstruction (continuity) metrics quantify performance across volunteers.

**Implementation parameters:** Electrode centroids were extracted via DBSCAN ($\epsilon$=0.47 cm, *min_ samples* =5). Frequency bands were isolated with a first-order zero-phase Butterworth filter. Spherical $k$-means ($K_U$=$K_B$=3, 60 iterations) defined the organ clusters; the first $r$=2 raw cluster vectors per opposing organ served as null columns. Shrinkage was set to $\beta$=0.10 with additional diagonal loading $10^{-3}\mathrm{tr}(\mathbf{R}_w)/M$. Overlap-add used 120 s Hann-tapered windows with 30 s steps (75% overlap).

## 3 Experiments and Results

The resulting dataset comprises ten paired abdominal EHG–MRI datasets (7 female and 3 male volunteers, 3 longitudinal recordings). In a cohort-level comparison of normalized PSDs between women and men, women exhibited consistent low-frequency uterine activity with well-defined components within the uterus band $[5, 50]$ mHz, while bladder-band activity $[25, 41]$ mHz appeared weaker and located within the broader uterine spectrum. In men, prominent peaks occurred in bladder-related and non-uterine regions. These sex-specific spectral patterns support applying uterus–bladder separation in women (Fig. 2 I).

The anatomical properties extracted via DOA clustering showed substantial inter-subject variability in the 10 processed datasets: uterus–bladder separation angles spanned approximately 13.1° to 37.6°, uterine cluster compactness ranged from 0.019 to 0.194, and bladder compactness from 0.062 to 0.246. Despite this variability, the LCMV pass constraint was consistently satisfied across

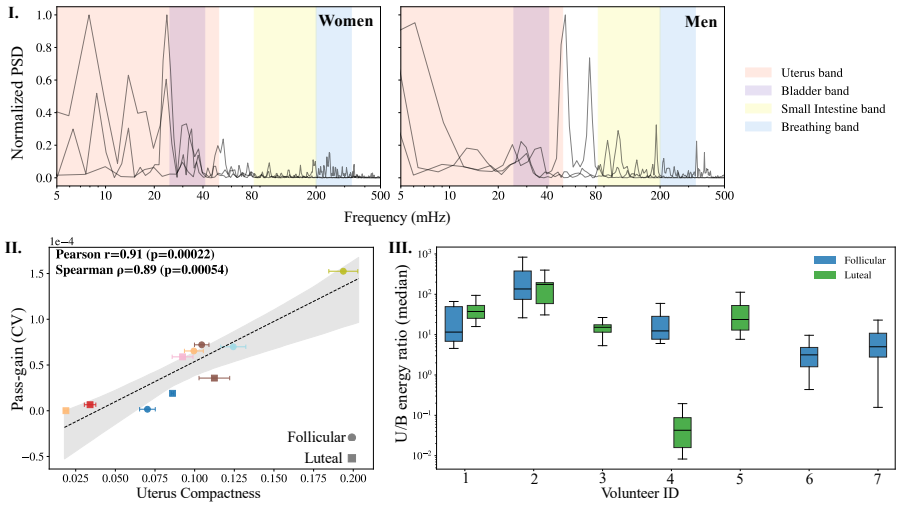


**Fig. 2. Group-level analysis. (I)** Normalized PSD across 3 randomly chosen female and 3 male volunteers, with uterine-band activity limited to females. **(II)** Uterus cluster compactness vs. pass-gain variability (coefficient of variation, CV), with one color per volunteer. **(III)** Median uterus-to-bladder energy ratio ($|yU|/|yB_{clean}|$) after leakage removal, showing stable organ-level separation.

sessions, with pass gains effectively at unity and subject-specific variability observed in null gains (approximately 0.10–0.48). These outcomes are summarized in Table 1 and demonstrate accurate pass-direction enforcement accompanied by anatomy-dependent cross-organ suppression. Across all volunteers, uterus compactness was strongly associated with pass-gain stability. Tighter uterus clusters exhibited minimal pass-gain fluctuation across windows, whereas more dispersed clusters produced higher variability. This relationship was strong and statistically significant (Pearson $r = 0.91$; Spearman $\rho = 0.89$). The three participants with longitudinal measurements, each scanned across follicular and luteal menstrual phases, aligned along the same region of the trend, confirming within-subject consistency across cycle phases. This provides clear evidence that uterus compactness, rather than separation angle, is the dominant geometric determinant of beamformer stability (Fig. 2 II). Median uterus-to-bladder energy ratio highlights inter-subject differences with stable within-subject behavior across sessions (Fig. 2 III). Leakage analysis further corroborates effective organ disentanglement. Across datasets, $|\alpha|$ remained $< 0.5$ for cases with compact uterine clusters (UT compactness $\lesssim 0.10$), and rose only when clusters were more dispersed, where larger coefficients appeared. In all cases, the correlation change after leakage subtraction $\Delta r$ was negative and energy ratio ($|yB_{clean}|/|yB|$) was $< 1$ (see Table 1), confirming the de-correlation of the bladder estimate of the removed component. These observations show successful removal of uterus-related contamination without compromising the bladder-band signal.

**Table 1.** Geometry, beamforming constraint, uterus–bladder separation and leakage metrics across all recordings. Values shown as mean±std or median.

| **Sub.** | **Phase** | **Separ. (°)** | **UT Comp.** | **BL Comp.** | **Null Gain** | $\lvert\alpha\rvert$ | $\Delta$**r** | **E Rat.** |
|---|---|---|---|---|---|---|---|---|
| 1 | Follic. | 35.8±9.6 | 0.070±0.005 | 0.105±0.006 | 0.210±0.049 | 0.28 | -0.563 | 0.684 |
| | Luteal | 37.6±6.8 | 0.086±0.001 | 0.103±0.006 | 0.231±0.036 | 0.20 | -0.582 | 0.787 |
| 2 | Luteal | 13.1±9.8 | 0.019±0.001 | 0.097±0.010 | 0.102±0.014 | 0.16 | -0.69 | 0.650 |
| | Follic. | 27.8±7.9 | 0.099±0.006 | 0.133±0.012 | 0.115±0.016 | 0.32 | -0.71 | 0.677 |
| 3 | Luteal | 13.2±5.5 | 0.034±0.004 | 0.062±0.008 | 0.238±0.007 | 0.13 | -0.15 | 0.961 |
| 4 | Luteal | 19.8±7.8 | 0.112±0.010 | 0.117±0.007 | 0.483±0.036 | 2.17 | -0.30 | 0.908 |
| | Follic. | 25.3±7.0 | 0.104±0.005 | 0.159±0.014 | 0.256±0.016 | 0.58 | -0.55 | 0.663 |
| 5 | Luteal | 27.3±7.6 | 0.092±0.007 | 0.246±0.020 | 0.167±0.056 | 0.36 | -0.64 | 0.729 |
| 6 | Follic. | 26.1±12.1 | 0.194±0.009 | 0.167±0.016 | 0.431±0.072 | 0.18 | -0.23 | 0.919 |
| 7 | Follic. | 34.9±11.2 | 0.124±0.008 | 0.217±0.006 | 0.287±0.025 | 0.34 | -0.27 | 0.920 |

A representative volunteer example illustrates the mechanism and robustness in-depth (Fig. 3). Supplementary video shows the dynamic MRI acquisition with the reconstructed uterus signal. The uterus beamformer exhibits strong responses to uterus clusters and deep suppression to bladder clusters, while the bladder beamformer shows the converse pattern. Figure 3 III reports mean cross-organ nulls of approximately $-155.5$ dB for uterus→bladder and $-158.7$ dB for bladder→uterus, reflecting stringent mathematical enforcement of the prescribed spatial constraints. The practically relevant cross-organ attenuation is captured by the null gain (0.10–0.48, Table 1), which reflects anatomy-dependent suppression of the undesired organ's contribution. Window-wise constraint residuals remain stable, with median pass residuals in the order of $10^{-12}$ and modest null residuals (Fig. 3 IV), confirming appropriate enforcement of pass and null constraints over time. Leakage diagnostics show a median $|\alpha| = 0.324$, a median $\Delta r = -0.709$ (de-correlation after subtraction), and a bladder energy ratio $\approx 0.68$, indicating leakage subtraction improving the bladder estimate while preserving organ-specific content. This aligns with the broader cohort behavior: anatomical compactness supports stable pass-direction performance, organ-level separability is primarily subject-specific, and leakage correction provides clean bladder estimates even under cross-organ contamination.

## 4 Discussion

A new approach to disentangle uterus and bladder contributions in paired EHG-MRI recordings with LCMV beamforming has been demonstrated. Despite wide variation in uterus–bladder separation angles, null suppression did not depend on macroscopic orientation. Instead, uterine cluster compactness strongly tracked pass-gain stability, compact clusters yielded near-constant pass responses—while dispersed clusters showed higher temporal variability— identifying subject-specific compactness as the dominant driver of pass-direction robustness. A scalar leakage subtraction further improved bladder isolation without destabilizing the

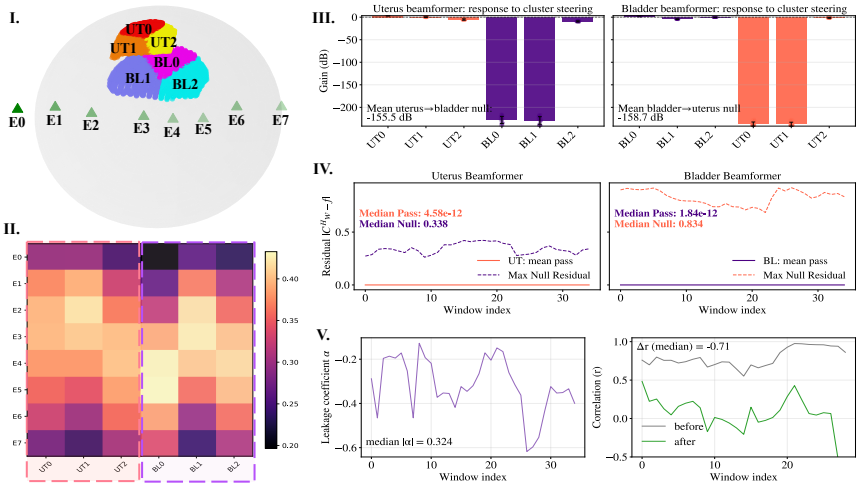


**Fig. 3. Subject-level analysis. (I)** Cluster labels for uterus (UT0–2) and bladder (BL0–2). **(II)** Steering-magnitude heatmaps across 8 electrodes with distinct profiles. **(III)** Beamformer response per cluster: targets near 0 dB, cross-organ clusters strongly suppressed. **(IV)** Constraint satisfaction: pass residuals near zero; max null residual tracks the largest remaining cross-organ response. **(V)** Low window-wise leakage and reduced correlation after subtraction indicates cross-organ contamination removal.

beamformer; all sessions had $\Delta r$ negative and bladder energy ratios $< 1$, and larger $|\alpha|$ occurred only with less-compact clusters, consistent with greater residual cross-organ coupling. These findings have practical implications for EHG system design. First, they suggest prioritizing electrode configurations and steering dictionaries that increase uterine cluster compactness—e.g., by individualizing sensor placement. Second, they support combining complementary explicit cross-organ nulls with dedicated leakage subtraction. Finally, the demonstrated performance with 8 channels indicates that constrained beamforming is feasible even when the number of sensors $M$ is far lower than the number of candidate directions $G$, provided anatomical priors and multi-cluster formulations are used. Regarding computational cost, manual MRI segmentation requires approximately 3 hours per subject; once the anatomical model is available however, the automated pipeline completes in under 1 min on a standard laptop. Current limitations include the modest cohort size composed of healthy participants and the opportunistic data acquisition with respect to menstrual-phase. The reported metrics—pass/null gains, $\Delta r$ , and energy ratios—quantify internal engineering consistency rather than independent physiological evidence of organ-level separation; larger prospective datasets and validation against independent references such as urodynamics or the concurrent EPI dynamic MRI are needed. Future work should also assess compactness via biomechanically informed surface metrics, evaluate adaptive electrode layouts, and investigate stability in pregnancy and pelvic floor disorders. Together, these results indicate

that anatomy-guided multicluster LCMV beamforming—augmented with leakage subtraction—provides a robust, subject-aware pathway for separating uterus and bladder activity in low-channel EHG.

## 5 Conclusion

We presented an anatomy-guided multicluster LCMV beamforming framework that disentangles uterus and bladder activity in paired EHG–MRI data. While uterus–bladder separation angles varied, null suppression did not depend on macroscopic orientation. Instead, uterine cluster compactness strongly predicted pass-direction stability, and a scalar leakage subtraction further improved bladder isolation without destabilizing the beamformer. These findings inform sensor placement and constraint design, showing feasibility with 8 channels when anatomical priors are used.

**Acknowledgments.** The authors thank Cilia from Brain Products for helping the project meet safety requirements. This work was supported by the High Tech Agenda of the Free State of Bavaria, DFG Heisenberg funding [502024488] and an ERC Starting grant EARTHWORM [101165242]. Code will be made publicly available upon publication. Participant data may be shared upon reasonable request, subject to institutional and ethical guidelines.

**Disclosure of Interests.** The authors have no competing interests to declare.

## References

1. Alberola-Rubio, J., Mira-Tomas, J.M., Diaz-Martinez, A., Alama Faubel, P., Caballero Sanz, S., Castillón Cortés, G., de Arriba-Garcia, M., Llácer, J., Garcia-Casado, J.: Objective and comprehensive characterization of uterine peristaltic activity throughout the menstrual cycle by means of intracavitary electrohysterography, a cohort study. Acta Obstet. Gynecol. Scand. **105**(1), 156–165 (2026). https://doi.org/10.1111/aogs.70088
2. Cai, C., Long, Y., Ghosh, S., Hashemi, A., Gao, Y., Diwakar, M., Haufe, S., Sekihara, K., Wu, W., Nagarajan, S.S.: Bayesian adaptive beamformer for robust electromagnetic brain imaging of correlated sources in high spatial resolution. IEEE Transactions on Medical Imaging **42**(9), 2502–2512 (2023). https://doi.org/10.1109/TMI.2023.3256963
3. Eytan, O., Halevi, I., Har-Toov, J., Wolman, I., Elad, D., Jaffa, A.J.: Characteristics of uterine peristalsis in spontaneous and induced cycles. Fertil Steril **76**(2), 337–41 (2001). https://doi.org/10.1016/s0015-0282(01)01926-4
4. Garfield, R.E., Maner, W.L.: Physiology and electrical activity of uterine contractions. Semin Cell Dev Biol **18**(3), 289–95 (2007). https://doi.org/10.1016/j.semcdb.2007.05.004
5. Harmsen, M.J., Trommelen, L.M., de Leeuw, R.A., Tellum, T., Juffermans, L.J.M., Griffioen, A.W., Thomassin-Naggara, I., Van den Bosch, T., Huirne, J.A.F.: Uterine junctional zone and adenomyosis: comparison of mri, transvaginal ultrasound and histology. Ultrasound Obstet Gynecol **62**(1), 42–60 (2023). https://doi.org/10.1002/uog.26117

6. Kido, A., Togashi, K., Nishino, M., Miyake, K., Koyama, T., Fujimoto, R., Iwasaku, K., Fujii, S., Hayakawa, K.: Cine mr imaging of uterine peristalsis in patients with endometriosis. Eur Radiol **17**(7), 1813–9 (2007). https://doi.org/10.1007/s00330-006-0494-9
7. Kuijsters, N.P.M., Methorst, W.G., Kortenhorst, M.S.Q., Rabotti, C., Mischi, M., Schoot, B.C.: Uterine peristalsis and fertility: current knowledge and future perspectives: a review and meta-analysis. Reprod Biomed Online **35**(1), 50–71 (2017). https://doi.org/10.1016/j.rbmo.2017.03.019
8. Kunz, G., Noe, M., Herbertz, M., Leyendecker, G.: Uterine peristalsis during the follicular phase of the menstrual cycle: effects of oestrogen, antioestrogen and oxytocin. Hum Reprod Update **4**(5), 647–54 (1998). https://doi.org/10.1093/humupd/4.5.647
9. Paramasivam, S., Proietto, A., Puvaneswary, M.: Pelvic anatomy and mri. Best Practice & Research Clinical Obstetrics & Gynaecology **20**(1), 3–22 (2006). https://doi.org/10.1016/j.bpobgyn.2005.09.001
10. Rabotti, C., Sammali, F., Kuijsters, N., Schoot, B., Kortenhorst, M., Mischi, M.: Analysis of uterine activity in nonpregnant women by electrohysterography: A feasibility study. In: 2015 37th Annual International Conference of the IEEE Engineering in Medicine and Biology Society (EMBC). pp. 5916–5919 (2015). https://doi.org/10.1109/EMBC.2015.7319738
11. Soares, D.M., Junior, H.W., Bittencourt, L.K., Lopes, F., de Oliveira, M.A.P.: The role of cine mr imaging in the assessment of uterine function. Arch Gynecol Obstet **300**(3), 545–553 (2019). https://doi.org/10.1007/s00404-019-05222-9
12. Wang, H., Wen, Z., Wu, W., Sun, Z., Kisrieva-Ware, Z., Lin, Y., Wang, S., Gao, H., Xu, H., Zhao, P., Wang, Q., Macones, G.A., Schwartz, A.L., Cuculich, P., Cahill, A.G., Wang, Y.: Noninvasive electromyometrial imaging of human uterine maturation during term labor. Nat Commun **14**(1), 1198 (2023). https://doi.org/10.1038/s41467-023-36440-0
13. Wang, S., Anderson, K., Pizzella, S., Xu, H., Wang, W., Wen, Z., Nan, Y., Lau, J., Wang, Q., Ratts, V., Wang, Y.: Noninvasive imaging of 4d electrical activation patterns of uterine peristalsis during normal menstrual cycles. npj Women's Health **2**(1) (2024). https://doi.org/10.1038/s44294-023-00003-x
14. Woolrich, M., Hunt, L., Groves, A., Barnes, G.: MEG beamforming using Bayesian PCA for adaptive data covariance matrix regularisation. NeuroImage **57**(4), 1466–1479 (2011). https://doi.org/10.1016/j.neuroimage.2011.04.041
15. Zahran, S., Yochum, M., Diab, A., Zahran, S., Marque, C.: Variation-based sparse source imaging in localizing uterine activity. In: Annual International Conference of the IEEE Engineering in Medicine and Biology Society (EMBC). pp. 2948–2951. IEEE (2017). https://doi.org/10.1109/EMBC.2017.8037475
16. Zahran, S., Alrifai, B., Diab, A., Khalil, M., Marque, C.: Separation and localization of ehg sources using tensor models. In: 2017 Fourth International Conference on Advances in Biomedical Engineering (ICABME). pp. 1–4 (2017). https://doi.org/10.1109/ICABME.2017.8167547